A statistical analysis of the influence of microstructure and twin–twin junctions on twin nucleation and twin growth in Zr

P.-A. Juan [a,c], C. Pradalier [b], S. Berbenni [c], R.J. McCabe [d], C.N. Tomé [d], L. Capolungo [a,*]

[a] G.W.Woodruff School of Mechanical Engineering, Georgia Institute of Technology, UMI GT-CNRS 2958, France
[b] Georgia Tech Lorraine, UMI GT-CNRS 2958, France
[c] Laboratoire d'Etude des Microstructures et de Mécanique des Matériaux LEM3, UMR CNRS 7239, University of Lorraine, Metz, France
[d] MST, Los Alamos National Laboratory, Los Alamos, NM 87545, USA

ARTICLE INFO

ABSTRACT

The purpose of the present work is (1) to study the statistical relevance of twin–twin junctions and (2) to study statistically the influence of twin–twin junctions and microstructure on nucleation and growth of twins in h.c.p. materials. A new automated twin recognition technique has been developed and is used to extract statistics from EBSD scans of high purity clock-rolled zirconium specimens loaded along the through-thickness and one of the in-plane directions. The technique allows for recognition of tensile and compressive twin systems within each individual grain. The ten possible twin–twin junction types that may occur in Zr between first generation twins are introduced as well as their associated frequencies in cases of through-thickness and in-plane compression. The present study shows that twin–twin junctions between twins belonging to the most active twinning modes are statistically relevant. It is also shown that twin–twin junctions hinder twin growth. In agreement with previous studies, it is found that irrespective of the loading direction and twin mode, both grain size and crystallographic orientation largely influence the propensity of grains for twin activation. However, the study suggests large differences in nucleation and growth mechanisms for each twinning mode.

© 2015 Acta Materialia Inc. Published by Elsevier Ltd. All rights reserved.

1. Introduction

High plastic anisotropy observed in hexagonal close-packed (h.c.p) metals arises from the activation of both twinning and slip systems [1–6]. In zirconium, twinning implies a reorientation of the lattice leading to a mirror image with respect to the twinning plane. $\{10\bar{1}2\}$ and $\{11\bar{2}1\}$ twins form when the c-axis is loaded in tension and $\{10\bar{1}1\}$ and $\{11\bar{2}2\}$ twins form when the c-axis is loaded in compression. Therefore, $\{10\bar{1}2\}$ and $\{11\bar{2}1\}$ twin modes are termed tensile while $\{10\bar{1}1\}$ and $\{11\bar{2}2\}$ are termed compressive [7–9]. Kaschner et al. [2] characterized experimentally the prevalent deformation mechanisms in Zr loaded along the through-thickness and one of the in-plane directions at liquid nitrogen and room temperatures. These mechanisms are prismatic slip, pyramidal slip and tensile twinning at room temperature and prismatic slip and tensile and compressive twinning at liquid nitrogen temperature. They show that the lattice reorientation induced by twinning softens the material when compression twins are

activated or hardens the material when tensile twins nucleate and grow [2].

Crystallography of twinning [10,11,1,12,13] is well understood and recent developments in the case of $\{10\bar{1}2\}$ twins have largely refined our understanding of twin growth. However, the contributions to mechanical response of interactions between slip modes [14,15], between slip and twin modes [16–20,5,21,22] and between twin modes on the mechanical response of h.c.p. metals remain less understood. Regarding slip system interaction, dislocation dynamics simulations of plastic deformation in Zr single crystals revealed that no junction is formed between screw dislocations gliding on different prismatic planes at low temperature, resulting in low strain hardening [23]. More recently, Juan et al. [24] introduced a double inclusion elasto-plastic self consistent scheme to study the effect of twin and parent domain interactions on slip system activation and hardening in the AZ31 Mg alloy. The direct coupling between parent and twin phases leads to an increase in hardening and hardening rate of twinned grains. Regarding twin–twin interactions, El Kadiri et al. [25] compared nucleation and growth of $\{10\bar{1}2\}$ twins in Mg AM30 in one grain containing one twin variant and in another grain containing two twin variants with approximately the same Schmid factor. It was

* Corresponding author.

suggested that twin intersections tend to increase the rate of nucleation events while decreasing the growth rate of individual twin lamella. Twin–twin intersections behaved as barriers counteracting further twin propagation and lead to higher strain hardening. Yu et al. [26,27] experimentally characterized three different $\{10\bar{1}2\}$ twin–twin junctions in Mg single crystals that had been cyclically loaded. These prior studies are all limited to $\{10\bar{1}2\}$ tensile twins.

Following an approach similar to the one used by [28,29], the purpose of the present work is to perform a complementary statistical study of the influence of twin–twin junctions, grain size and grain orientation of twinned grains on nucleation and growth of all twins. To this end, a new automated twin recognition technique [30], based on graph theory analysis, is developed and used on electron backscatter diffraction (EBSD) data obtained from clock-rolled high-purity Zr. First the experimental data collected in Capolungo et al. [28] and pertaining to in-plane loading at 76 K of clock rolled Zr is revisited. Second, to assess the generality of these results, additional experimental data are collected for the same material and loading direction. Finally, new experiments on Zr loaded in compression along the through thickness direction are performed and scans are studied in order to analyze compressive twins, their mutual interactions and their interactions with tensile twins.

The first section is dedicated to the experimental procedure and material characteristics. The second section introduces a nomenclature to describe all possible twin–twin junctions in Zr and presents their associated statistics. In the last section, the influence of grain size, crystallographic orientation and twin–twin junctions on nucleation and growth of twins is discussed.

2. Experimental procedure and material characteristics

2.1. Experimental procedure

The material used comes from a high-purity crystal bar Zr (<100 ppm) which was arc-melted, cast and clock-rolled at room temperature. Cuboidal samples were machined from the rolled plate and annealed at 823 K for 1 h. In the as-annealed state, grains are free of twins, equiaxed and have an average diameter equal to 17 μm. Specimens display a strong axisymmetric texture where basal poles are aligned within approximately 30 degrees of the through-thickness direction (Fig. 1). Samples were deformed in an equilibrium liquid nitrogen bath at 76 K in order to facilitate twin nucleation and loaded in compression along one of the in-plane directions to 5% strain (IP05) and along the through-thickness direction to 3% strain (TT03). Fig. 2 shows the macroscopic stress–strain curves of cubes compressed along the through-thickness (TT) and in-plane (IP) directions.

Experimental data were collected from 10 and 4 (240 μm × 120 μm) scans at different locations on the same cross
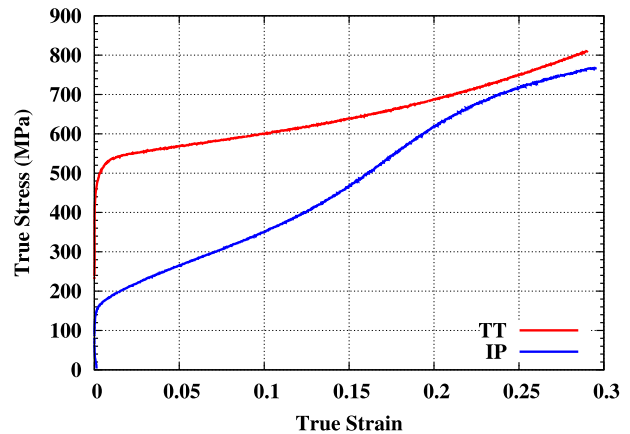

Fig. 2. Macroscopic stress–strain curves of high purity Zr samples loaded in compression along through-thickness (TT) and in-plane (IP) directions at 76 K and 300 K.

sectional area of the TT03 and IP05 samples (Fig. 3), respectively. The section plane for TT03 analysis contains both the TT direction and IP direction, and the section plane for IP05 analysis contains the TT direction and the IP compression direction. Statistical data were obtained using the automated EBSD technique developed by Pradalier et al. [30]. The total analyzed area for TT03 and IP05 specimens is 205,736 μm² and 73,122 μm², respectively. Twins represent 9.1% and 5.7% of the total scanned area in TT03 and IP05 samples, respectively. Incomplete grains bounded by scan edges are not considered in the statistical analyses.

Computing misorientations between measurement points and relying on graph theory analysis, the twin recognition EBSD software [30] is able to identify the four twin modes present in Zr (Table 1). As highlighted by recent studies [2,28], $\{11\bar{2}2\}$ compressive (C_1) twins and $\{10\bar{1}2\}$ tensile (T_1) twins are the most commonly observed twins in TT03 and IP05 scans, with 74.4% and 81.7% respectively (Table 2). Table 2 also reveals that the second most active twinning modes are $\{10\bar{1}2\}$ (T_1) and $\{11\bar{2}1\}$ (T_2) in TT03 and IP05 samples, respectively. In both cases, the second most active twin modes represent about 17% of the total number of twins. However, no $\{10\bar{1}1\}$ (C_2) twin has been observed in 14 scans.

Grain areas are directly calculated from the number of experimental points of the same orientation with a step size, equal to 0.2 μm. As a result of the annealing treatment the grains are equiaxed. Grain area is computed by multiplying the number of measurement points that the grain contains by the area associated with a pixel, i.e. 0.1 μm². Grain diameter is estimated assuming a spherical grain. The software developed by Pradalier et al. [30] fits an ellipse to each twin. The measured twin thickness is defined as the minor axis of the ellipse. The true twin thickness is then estimated by multiplying the measured twin thickness by the cosine of the angle formed by the twin plane, K_1, and the normal to the sample surface [31,29]. Because EBSD scans do not provide access to local stresses before unloading and sectioning, for classification purposes the geometric Schmid factors (SF) are computed from the inner product of the symmetric Schmid tensor and the normalized macroscopic stress tensor, such that $\|\Sigma\|^2 = \sum_{i=1}^{3}\sum_{j=1}^{3}\Sigma_{ij}^2 = 1$. In addition, similar statistics using the macroscopic stress for computations of distributions can be produced from the use of either full-field or mean field models. The symmetric Schmid tensor is defined as the symmetric part of the dyadic product between the Burgers vector and the normal vector to the deformation plane. For each twinned grain, the six possible twin variants of each twinning mode are classified in order of decreasing SF.
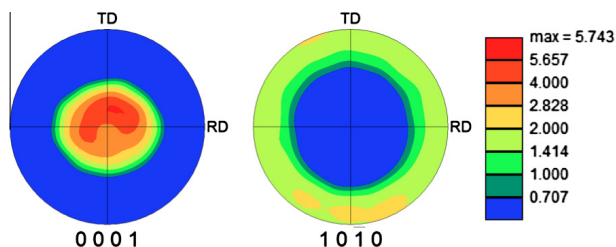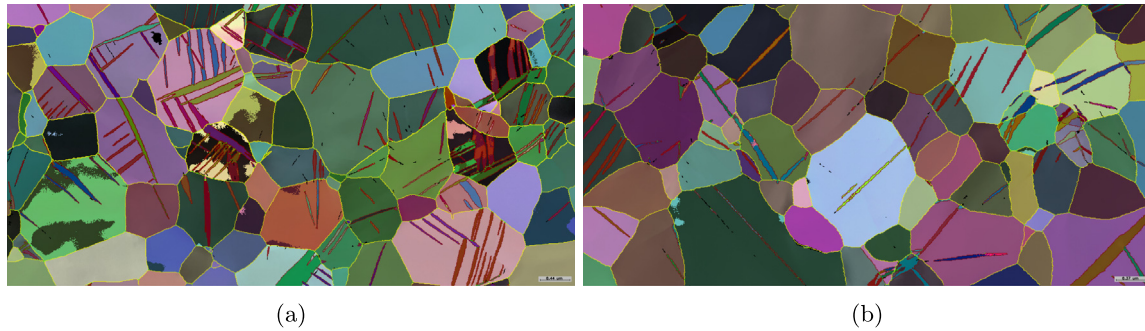

Fig. 1. Initial basal $(0\,0\,0\,1)$ and prismatic $(1\,0\,\bar{1}\,0)$ pole Figures of the clock-rolled high-purity zirconium studied in this work. The 3-axis is the through thickness direction of the plate.

Fig. 3. Examples of EBSD scans for specimens loaded in compression along the TT (a) and along one of the IP (b) directions.

Table 1
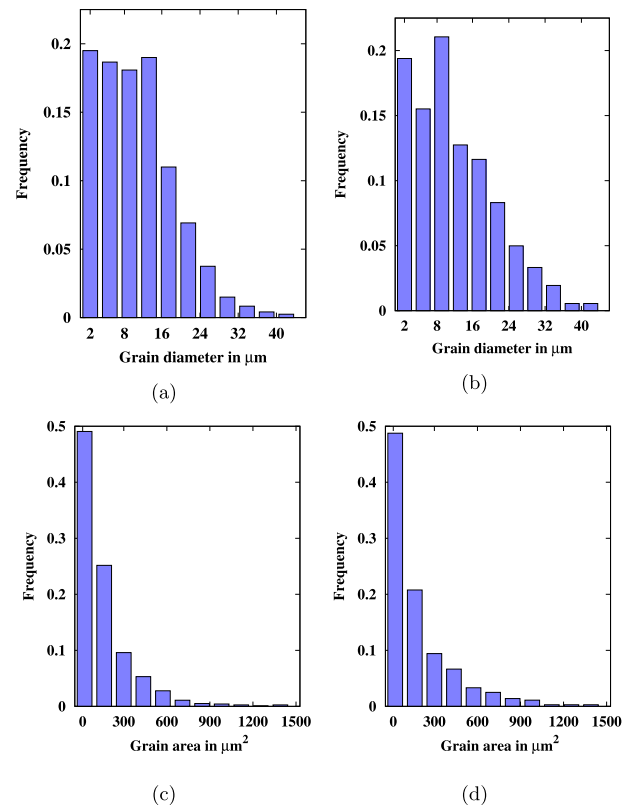Twinning modes in Zr. $\{10\bar{1}1\}$ (C_2) twins were not observed.

Abbreviation	Twinning plane, K_1	Twinning direction, η_1	Misorientation (deg)
T_1	$\{10\bar{1}2\}$	$\langle\bar{1}011\rangle$	85.2
T_2	$\{11\bar{2}1\}$	$\langle\bar{1}\bar{1}26\rangle$	34.9
C_1	$\{11\bar{2}2\}$	$\langle 11\bar{2}3\rangle$	64.2
C_2	$\{10\bar{1}1\}$	$\langle 10\bar{1}2\rangle$	57.1

While we can only detect fully formed twins with EBSD, their presence implies previous nucleation of such variants. To study twin nucleation, all grains (i.e. twinned and untwinned) that are not on the edge of the map are considered. Concerning twin growth, statistics are based on twinned grains solely. Fig. 4 shows grain diameter and area distributions of specimens loaded along the TT and IP directions. Because the notion of "grain" is questionable for very small number of measurement points, grains smaller than 4 μm² (i.e. 23 measurement points) are disregarded. In the following, data are represented as histograms. Histograms are very useful statistical tools for representing data and estimating density functions. But, they do not directly address the issues of bias and variance. However, it is still possible to minimize the error introduced by the histogram representation. In the present article, bin sizes are estimated from Scott's formula: $w = 3.49\sigma \cdot n^{-1/3}$ [32], where σ is an estimate of the standard deviation and n the number of elements considered, i.e. the total number of grains. The term $n^{-1/3}$ results from the minimization of the integrated mean squared error function. The main advantage of this expression lies in its insensitivity to the nature of the estimated density function (Gaussian, log normal, etc). Mean and standard deviation have been computed for area, diameter and SF distributions in TT03 and IP05 specimens. As a result, optimal bin widths for diameter, area and SF in TT03 samples are 63 μm², 2.5 μm and 0.06, respectively, and 112 μm², 4.1 μm and 0.06, respectively, in the case of IP05 maps. However, to be able to compare results obtained from

Fig. 4. Effective grain diameter (a,b) and grain area (c,d) distributions for TT03 (a,c) and IP05 (b,d) samples.

both TT03 and IP05 maps, the same bin sizes have to be applied. In addition, we enforced that all distributions expressed with respect to diameter and area have the same number of bins and that every bin contains at least one element. Consequently, diameter and bin sizes used in the next histograms are 5.47 μm and 132 μm², respectively. To avoid any empty column, one grain larger than 1456 μm² observed in a TT03 scan was disregarded. Concerning distributions plotted with respect to Schmid factor, the bin size was rounded down to 0.05 in order to obtain an exact integer number of subdomains between −0.5 and 0.5.

3. Twin–twin junctions statistics

This section is dedicated to the description of twin–twin junctions between first generation twins occurring in Zr. As mentioned in the previous section, 4 different twin modes are reported for Zr, which allows for 10 different junction modes. However, since only

Table 2
Statistical data for twinned grains and twins in deformed TT03 and IP05 samples.

Loading path	TT03		IP05	
Twin and grain type	Number	Frequency (%)	Number	Frequency (%)
All grains	1200	–	361	–
Twinned grains	530	–	197	–
All twins	1975	100	514	100
T_1 - $\{10\bar{1}2\}$	326	16.5	420	81.7
T_2 - $\{11\bar{2}1\}$	178	9.0	90	17.7
C_1 - $\{11\bar{2}2\}$	1471	74.5	3	0.58

3 twinning modes have been observed, 6 different twin–twin junction modes may occur. These are listed in Table 3. Depending on the twinning modes involved, each twin–twin junction mode contains 3 or 4 types. The distinction between the different twin–twin junction types is based on the value of the minimum angle formed by twin zone axes. Twin zone axis is here used to define the direction that is perpendicular to both the K_1 plane normal and the twinning shear direction, η_1. For example, 3 different types of $T_1 - T_1, T_2 - T_2$ and $C_1 - C_1$ junctions exist: the first one corresponds to junctions between two twins sharing the same zone axis; the second and third types correspond to junctions between twins for which the minimum angle formed by the two axes is equal to $2\pi/3$ and $\pi/3$ radians, respectively. In the case of $T_2 - C_1$ twin–twin junctions, 4 types of junctions are considered: 2 types corresponding to junctions between twins sharing the same zone axis and 2 other types for junctions between twins with non parallel zone axes. In the case of $T_1 - T_2$ and $T_1 - C_1$, 3 different types of junctions can be distinguished. None of them corresponds to junctions between twins with parallel zone axes. Minimum angles formed by twin zone axes are here equal to $\pi/6, \pi/2$ and $\pi/3$ rad. The 19 interaction modes and types observed in TT03 and IP05 scans are graphically represented in the Appendix A.
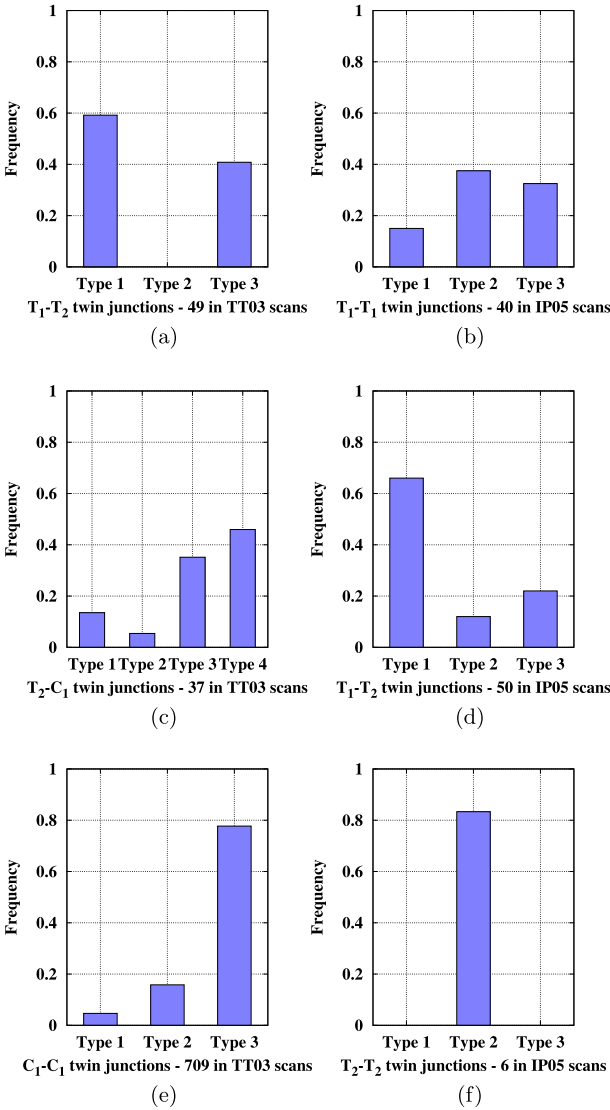
The total number of twin–twin junctions observed in TT03 and IP05 scans is 833 and 96, respectively. Table 3 lists all possible twin–twin junction modes in Zr, and, more relevant to this work, their observed occurrence frequencies. Frequencies are here defined as the ratio of the population of a given species to the overall population. Tables 2 and 3 show that in the case of specimens loaded along the through-thickness direction, whereby C_1 twins are most frequently observed, i.e. 74.5% of all twins, C_1 twins interact mostly with other C_1 twins. Furthermore, T_2 twins tend to interact with twins of different modes regardless the predominant mode since $T_2 - T_1, T_2 - C_1$ and $T_2 - T_2$ twin–twin junctions represent 5.9%, 4.5% and 1.4% of all junctions appearing in TT03 maps and 52.1%, 0% and 6.2% of all junctions observed in specimens loaded along the in-plane direction (IP05), respectively. In TT03 specimens, T_1 twins represent 16.5% of all twins (Table 2) but are only involved in 8.8% of all twin–twin junctions; they also represent 31.4% of all twins embedded in single twinned grains (Table 4). Even when parent grains are suitably well oriented for T_1 twin nucleation, such as in the case of compression along the IP direction, $T_1 - T_1$ twin–twin junctions only represent 41.7% of all twin–twin junctions while T_2 twins, whose population is 4.7 times smaller, are involved in 58.3% of all twin–twin junctions. For both TT and IP specimens, the ratio of twins belonging to the most active twinning mode to the number of twins belonging to the second most active twinning mode is similar, i.e. 4.5 and 4.6, respectively. However, no statistical trend appears regarding the 3 types of twin–twin junctions that may occur between the first and second most active twinning modes.

Table 3
Twin–twin junction frequencies for samples loaded in compression along the TT and IP directions.

Loading path		TT03		IP05	
Type number	Twin–twin interaction type	Number	Frequency (%)	Number	Frequency (%)
1	$T_1 - T_1$	19	2.3	40	41.7
2	$T_1 - T_2$	49	5.9	50	52.1
3	$T_1 - C_1$	5	0.6	0	0.0
4	$T_2 - T_2$	12	1.4	6	6.2
5	$T_2 - C_1$	37	4.5	0	0.0
6	$C_1 - C_1$	709	85.5	0	0.0

Table 4
Frequencies of twins contained in single twinned grains for TT03 and IP05 samples.

Loading path	TT03		IP05	
Twin category	Number	Frequency (%)	Number	Frequency (%)
All single twinned grains	176	–	73	–
T_1	55	31.4	62	84.9
T_2	18	10.3	8	11.0
C_1	102	58.3	3	4.1

Fig. 5. Modes and types of twin–twin junctions observed in EBSD scans of samples loaded along the TT-direction ((a), (c), (e)) and the in-plane directions ((b), (d), (f)).

Fig. 5 shows twin–twin junction types for each mode whose frequency is greater than 4% in TT03 (Fig. 5(a), (c) and (e)) and IP05 (Fig. 5(b), (d) and (f)) scans. Notations are all detailed in the Appendix A. Therefore, Fig. 5(e) shows that, in the case of through thickness compression, 80% of $C_1 - C_1$ twin–twin junctions correspond to the third type of junctions. Fig. 5 also reveals that junctions between $T_1 - T_1$ twins with parallel zone axes, studied by Yu et al. [26,27] in Mg single crystals, do not correspond to the predominant type of twin–twin junctions here. Results are purely qualitative but they can be used as guidelines for molecular dynamic simulations by highlighting what type of twin–twin
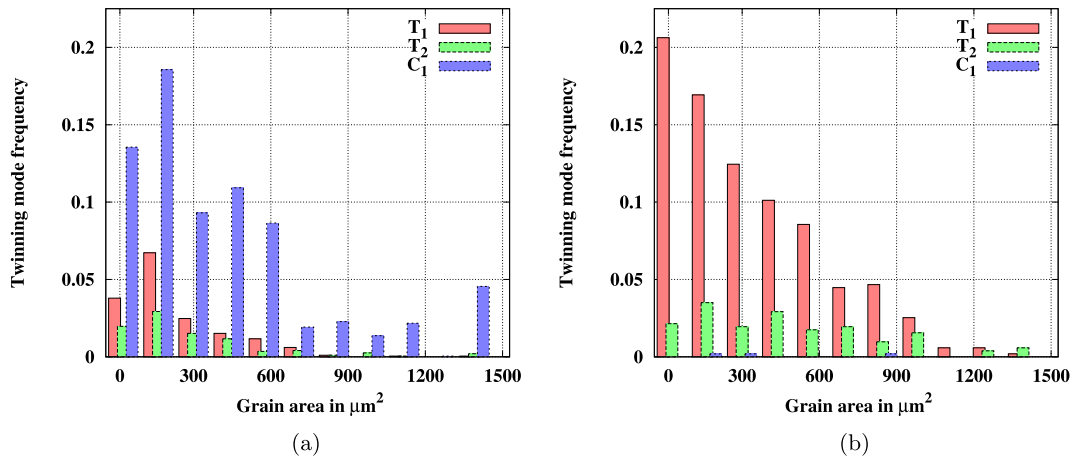
Fig. 6. Distribution of frequencies of T_1, T_2 and C_1 twins with respect to grain size in samples loaded along the TT (a) and the IP (b) directions.
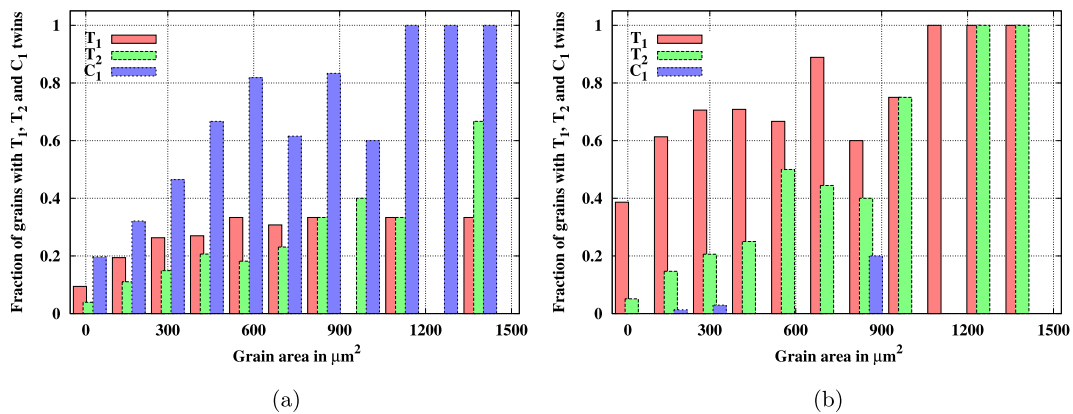

Fig. 7. Distribution of the fraction of twinned grains containing T_1, T_2 and C_1 twins plotted with respect to twinned grain area for samples loaded along the TT (a) and the IP (b) directions.

junctions should be considered for a given microstructure and loading path.

4. Influence of twin–twin junctions and grain-scale microstructural characteristics on twin nucleation and twin growth

The twinning process should be decomposed into three steps, starting with twin nucleation. The latter generally occurs at grain boundaries or local defects where internal stresses are highly concentrated. The second step corresponds to transverse propagation across the grain. Like a crack, the newly formed twin propagates very quickly until reaching another grain boundary or defect. Then, the third and last step is twin growth, consisting of twin thickening [33]. This section is dedicated to the study of statistics related to twin nucleation and twin growth. However, prior to any result and as a complement to Table 2, Figs. 6 and 9 present the distribution of twinning mode frequencies with respect to grain size and Schmid factor for specimens loaded along the TT and IP directions. Twinning mode frequencies are defined as the number of T_1, T_2 and C_1 twins contained in grains belonging to a given subdomain divided by the total population of twins. Notice that the larger number of twins associated with smaller grains should not be interpreted as a "reverse" Hall–Petch effect. Rather, it is a consequence of having a large number of small grains, as shown in Fig. 4. Figs. 4, 6 and 9 also indicate that certain bars are only representative of a few twins or a few grains. But, since most of statistics presented in this section rely on average

values, the authors decided to not plot bars corresponding to averages performed over less than 3 twins and 3 twinned grains in histograms displaying average twin thicknesses and average twin numbers per twinned grain, respectively.

4.1. Twin nucleation

Fig. 7 shows the evolution of the fraction of twinned grains containing T_1, T_2 and C_1 twins as a function of grain area. Similar to previous statistical studies performed in Mg and Zr [28,29], the present work also finds that twin nucleation can be correlated to grain size. However, Fig. 7 not only establishes that the overall probability of twinning incidence increases with grain area but also differentiates the 3 cases corresponding to the different twinning modes observed in samples loaded in compression along the TT and IP directions. The influence of grain size on nucleation probability appears to be the strongest for C_1 and T_1 twins in TT03 and IP05 scans, respectively, since 100% of grains larger than 1060 μm^2 contain at least one twin of the predominant twinning mode while less than 50% of grains smaller than 136 μm^2 are twinned. In both TT03 and IP05 specimens, the effect of grain size on T_2 twin incidence is significant. The fraction of grains containing at least one T_2 twin increases rapidly and linearly with grain area, even if, in the case of samples compressed along the TT direction, T_2 does not correspond to the second most active twinning mode. Still note that about 10% of grains smaller than 136 μm^2 and 30% of grains larger than 664 μm^2 contain at least one T_1 twin in TT03 scans.
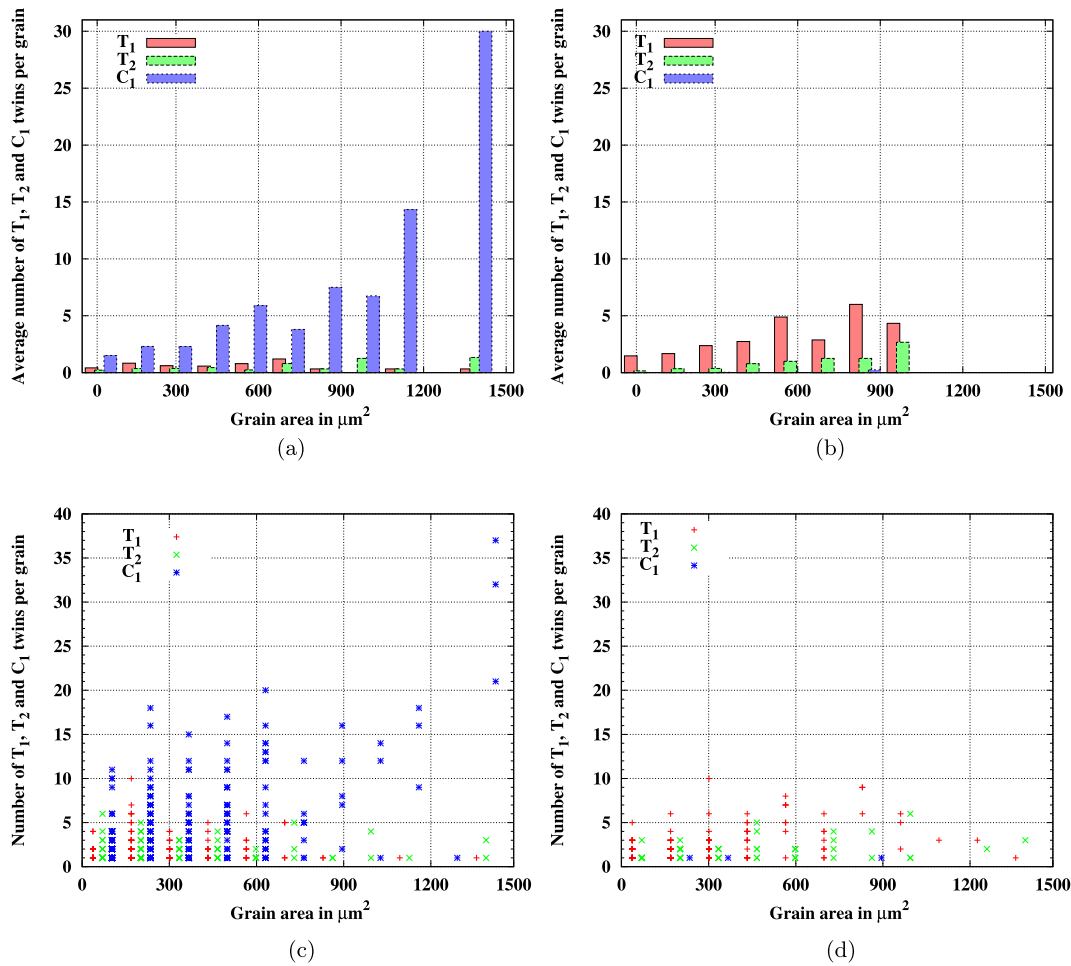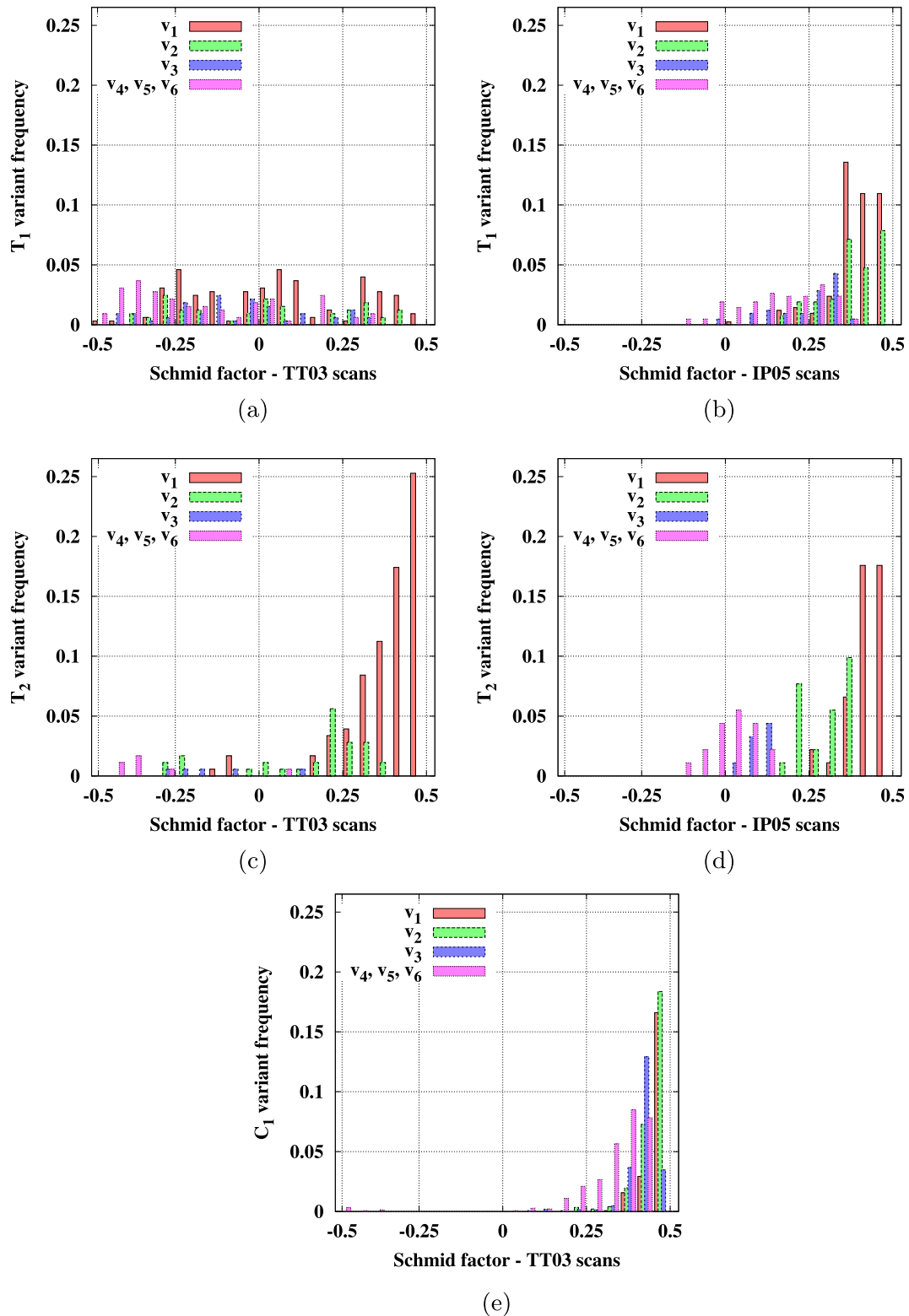
Fig. 8. Distribution of the number of T_1, T_2 and C_1 twins per twinned grain for TT03 (a) and IP05 (b) samples and scattergraphs displaying the number of C_1, T_2 and C_1 twins embedded in parent phases with respect to twinned grain area for TT03 (c) and IP05 (d) samples. Each cross represents one single twin. But because twin numbers are integers, many crosses overlap.
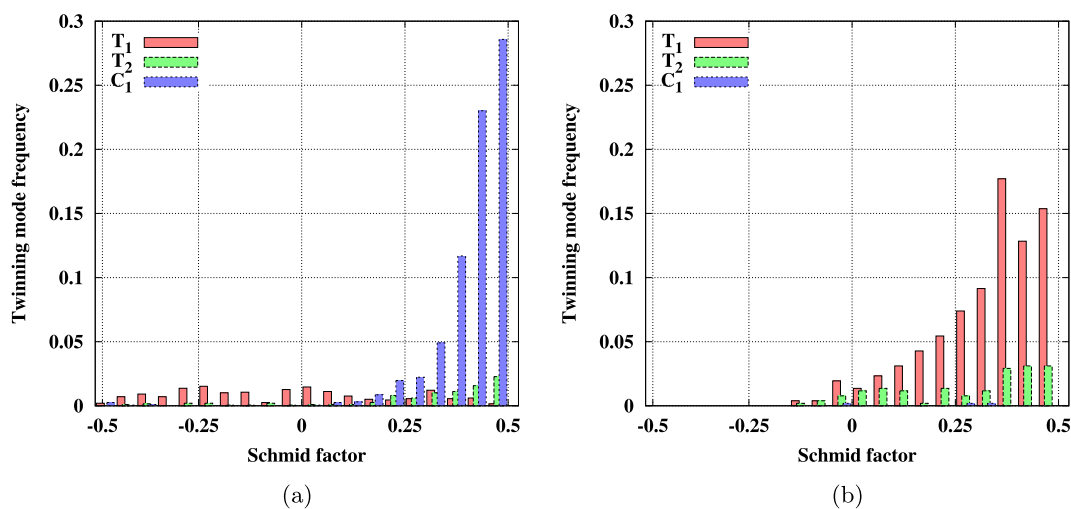
Fig. 9. Distribution of SF values corresponding to twins activated in samples loaded along the TT-direction (a) and the IP-direction (b).

Fig. 8 shows the distributions of the number of T_1, T_2 and C_1 twins per twinned grain with respect to grain size. While Fig. 8(a) and (b) are histograms displaying averaged values, i.e. averaged numbers of twins, Fig. 8(c) and (d) are scattergraphs displaying all values. Fig. 8(a) and (b) clearly reveal that the average number of twins belonging to the predominant twinning mode increases with grain size. The phenomenon is more pronounced for C_1 twins in samples loaded in compression along the TT direction.

Fig. 10. Distribution of variant frequencies of T_1 (a), T_2 (c) and C_1 (e) twins in TT03 scans and of T_1 (b) and T_2 (d) in IP05 scans, respectively, with respect to their Schmid factor. Variant frequencies consist in the ratio of the number of twins of a given SF variant and of a given twinning mode to the total population of twins belonging to the considered twinning mode.

However, the influence of grain size remains significant in the case of IP05 specimens: the average numbers of T_1 twins contained by grains whose areas are in the range [4 μm^2, 136 μm^2] and [534 μm^2, 664 μm^2] are equal to 1.5 and 4.9, respectively. This trend seems to change for grains larger than 928 μm^2. However, Fig. 6(b) indicates that beyond 796 μm^2 averages are performed over less than 5 grains. The interest of Fig. 8(c) and (d) lies in the observation that small grains can contain a very large number of

Table 5
Twins with negative SF and their relative frequencies and twinned areas in TT03 and IP05 samples

Loading path	TT03			IP05		
Twin mode	Number of twins	Rel. frequency (%)	Rel. twinned area (%)	Number of twins	Rel. frequency (%)	Rel. twinned area (%)
All	211	10.7	3.9	22	4.3	4.9
T_1	180	55.2	43.7	14	3.3	0.6
T_2	20	11.2	8.4	7	7.7	19.5
C_1	8	0.5	0.2	1	33.3	68.2

twins. It also shows that the number of twins per twinned grain can vary significantly from one grain to another. However, EBSD scans are images of 2D sections. As a result, it is possible that small grains are actually bigger than they seem to be. This introduces a bias in grain size effect statistics.

Nucleation of twins belonging to the predominant twinning mode is strongly controlled by grain orientation and macroscopic stress direction. As indicated by a classic Schmid factor analysis (Fig. 9), 91% and 76% of C_1 and T_1 twins, respectively, have a Schmid factor greater than 0.25. Fig. 10 also shows that 21% and 42% of C_1 and T_1 twins observed in specimens loaded along the TT and IP directions correspond to the 1st Schmid factor variant, denoted by v_1, respectively. Regarding the activation of twins belonging to the second most active twinning mode, the dependence on grain orientation and loading direction is less obvious.

The phenomenon is particularly striking in the case of T_1 twins in TT03 specimens since 55% of T_1 twins exhibit a negative Schmid factor (Table 5) and 26% of them correspond to either the 4th, 5th or 6th variants. For T_2 twins observed in IP05 scans, 38% have a Schmid factor lower than 0.25 and 20% correspond to either the 4th, 5th or 6th variants. Fig. 9 and Table 5 also reveal that the proportion of T_2 twins with a negative Schmid factor remains low (i.e. 11% and 8% in the case of TT and IP compressions, respectively) irrespective of the loading direction. The activation of twins with negative SF is a result of using the macroscopic stress to define SF. In practice, such a result is pointing at large local deviations from the macroscopic stress in the grains involved. Shi et al. [34] also suggested in a deformed AZ31 Mg alloy, i.e. AZ31, different strain accommodation mechanisms due to slip or twinning in the neighborhood of twins with low SF.
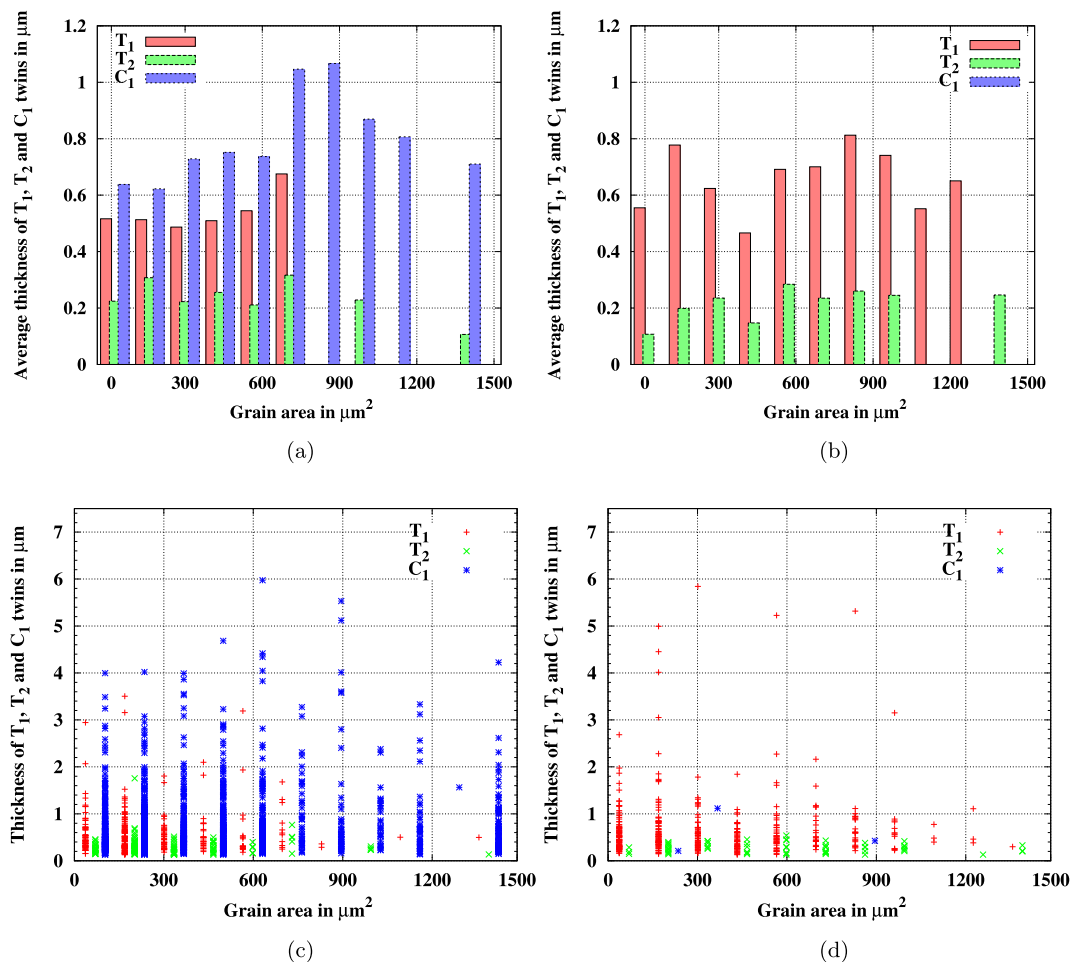
Fig. 11. Distribution of average twin thicknesses as a function of grain size in samples loaded along the TT (a) and the IP (b) directions and scattergraphs displaying twin thickness values with respect to grain size in samples loaded along the TT (c) and the IP (d) directions. Each cross represents one twin.
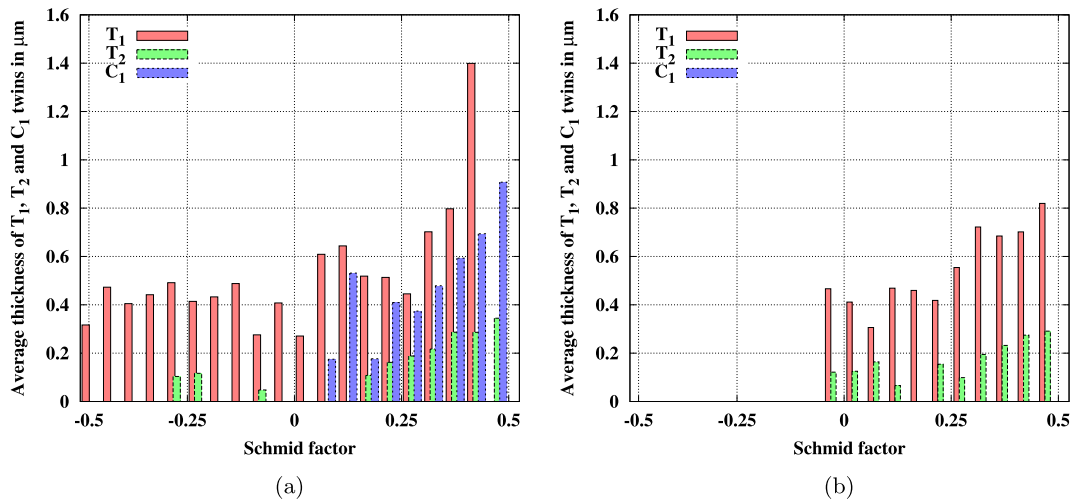
Fig. 12. Distribution of average twin thicknesses as a function of SF values in samples loaded along the TT (a) and the IP (b) directions.
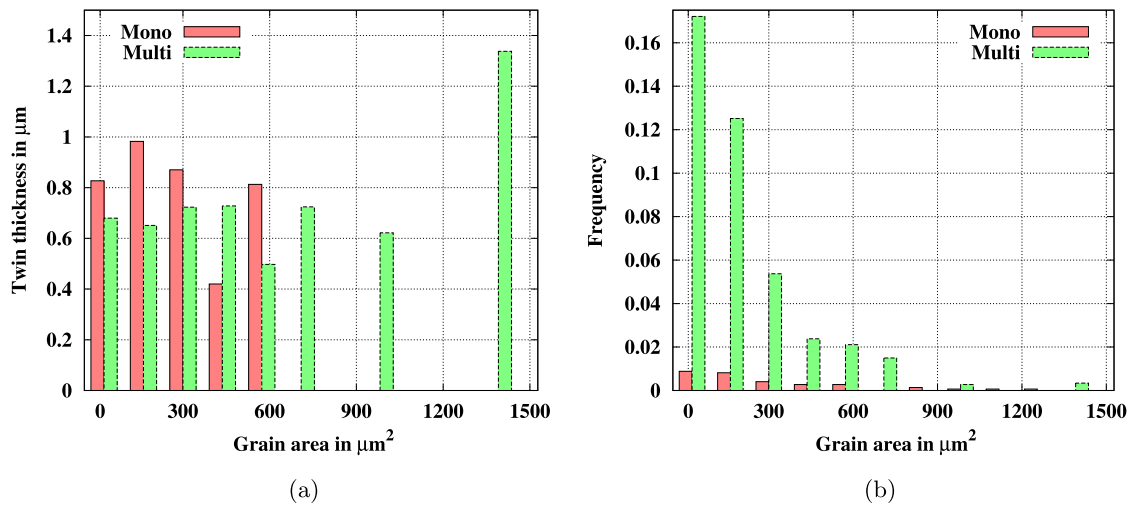

Fig. 13. Distribution of the twin thickness (a) and the frequency (b) of C_1 twins with respect to grain area in samples loaded along the TT direction.
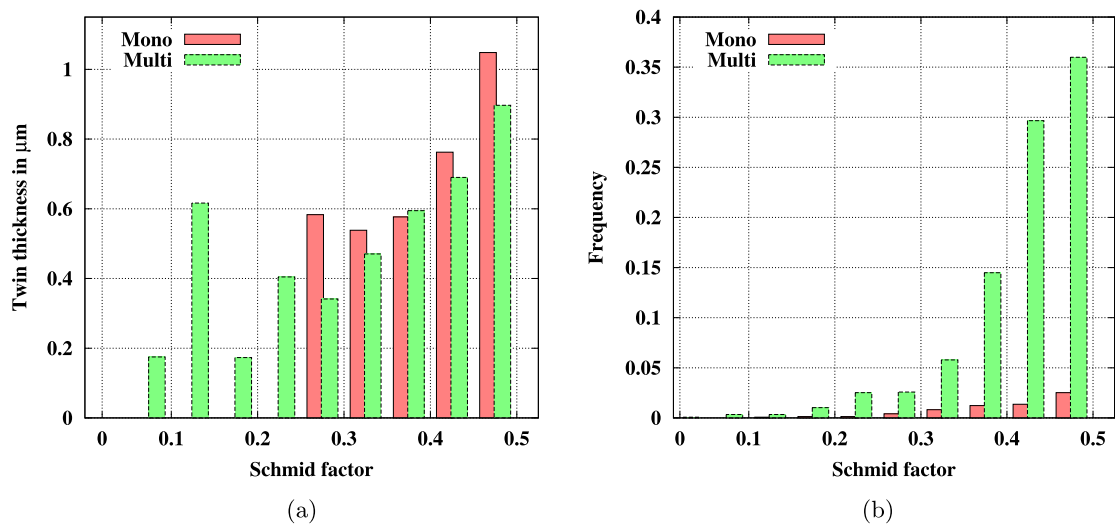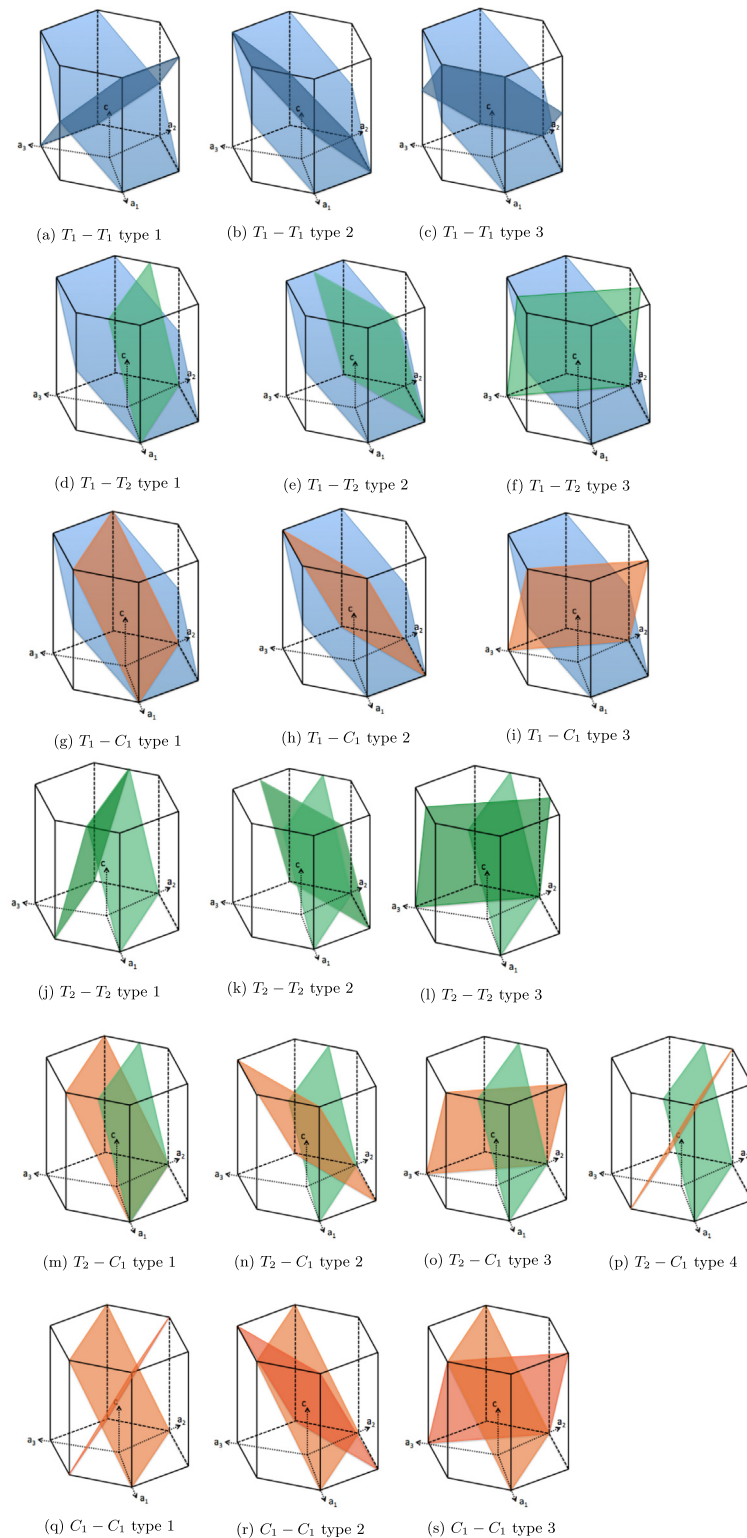

Fig. 14. Distribution of the twin thickness (a) and the frequency (b) of C_1 twins with respect to SF values in samples loaded along the TT direction.

Fig. 15. Graphical representation of twin–twin junction modes and types observed in TT03 and IP05 Zr EBSD scans. Schematic representation of twin–twin junction modes and types observed in TT03 and IP05 Zr EBSD scans.

4.2. Twin growth

Twin growth is considered as the last step in the twinning process consisting in twin lamella thickening. The influence of grain orientation, grain size and twin–twin junctions is investigated via histograms presenting twin thickness distributions with respect to grain area and Schmid factor. Following the same approach as the one used for twin nucleation, Fig. 11 shows statistics of twin true thicknesses as a function of grain size. Fig. 11(a) and (b) are histograms displaying average twin true thicknesses sorted by twinning mode. In the case of the TT compression, T_1 twin thickness average is always close to 0.5 μm. The value of C_1 average

twin thickness appears to first increase until grain size reaches 928 μm² and then decreases; the values corresponding to the first and last bin are 0.64 and 0.71 μm, respectively. In the case of the IP compression, T_1 twin thickness average oscillates around 0.75 μm. As a result, it is not possible to identify a correlation between twin thickness, twinning mode and twinned grain area. However, Fig. 11 also reveals that the average thickness of twins belonging to the most active mode is always greater than the average thickness of twins belonging to the second most active mode. Fig. 11(c) and (d) consist in scattergraphs that display all true thicknesses of twins observed in samples loaded along the TT and IP directions. The spread is significant and does not follow any pattern. Fluctuations may be associated with neighbor effects on twin growth. Numerical support for such effects is provided by Kumar et al. [33] and based on shear accommodation and stress considerations. Large thickness values observed in small grains also suggest that using 2D variables to describe spatial phenomena introduces a bias in grain size effect statistics. The same comment was made in the paragraph dealing with twin nucleation.

Disregarding negative Schmid factor twins (Fig. 9), the influence of the crystallographic orientation on the growth of twins belonging to the predominant mode is clearly shown in Fig. 12. Fig. 12 presents the distribution of twin thickness sorted by twinning mode with respect to Schmid factor. The average true twin thickness of C_1 and T_1 twins increases with increasing Schmid factor values in TT03 and P05 specimens, respectively. This indicates that the macroscopic stress is the major driving force for twin growth in the case of first most active twinning modes. However, similar to observations made about twin nucleation, the influence of grain orientation and macroscopic stress direction is reduced for twins belonging to the second and third most active twinning modes. As a result, mechanisms involved in the growth of twins belonging to the predominant twinning mode are likely to be different from those responsible for the growth of other twins. Beyerlein et al. [29] and Capolungo et al. [28] argue that if backstresses induced by neighboring grains in reaction to the localized twin shear are independent of orientation, then twins with higher SF, and hence with higher resolved shear stress, have an advantage to overcome this shear reaction.

Finally, to highlight the influence of twin–twin junctions on twin thickening in a statistically meaningful manner, the comparison of twin thicknesses between single twinned (also referred to as mono-twinned grains in Figs. 13 and 14) and multi-twinned grains is performed for C_1 twins in TT03 specimens. A multi-twinned grain is, here, defined as a twinned grain containing several twins. In the TT03 scans, 102 and 1369 twins in single twinned and multi-twinned grains were observed, respectively (see Tables 2 and 4). Figs. 13(b) and 14(b) show the distribution of twins embedded in single twinned and multi-twinned grains as a function of grain area and Schmid factor. They are aimed at indicating the statistical relevance of data about twins contained by single twinned grains. Fig. 14(a) presents the distribution of averaged twin thicknesses embedded in both single twinned and multi-twinned grains as a function of Schmid factor values. The Figure clearly shows that the average twin thickness of twins embedded in single twinned grains is greater or equal than the average twin thickness of twins contained by multi-twinned grains irrespective of grain orientation. This phenomenon appears more clearly for high and mid-high Schmid factor values, i.e. $SF > 0.25$. As previously mentioned, Fig. 14(b) shows that bars associated with negative Schmid factors apply to only a few single twinned grains. Moreover, Fig. 14(a) shows that similar to multi-twinned grains thickness of twins contained in single twinned grains does not depend on grain area. However, the latter is generally greater than the average twin thickness of twins in multi-twinned grains.

Fig. 13(b) also shows that almost all the single twinned grain areas are smaller than 664 μm². Such a result was expected due to the influence of grain size on twin nucleation.

5. Conclusion

The present work presents a statistical study performed on large set of EBSD scans of high purity Zr that discusses the influence of twin–twin junctions between first generation twins, grain size and crystallographic orientation on nucleation and growth of twins. Samples were loaded in compression at liquid nitrogen temperature along the through-thickness and one of the in-plane directions in order to favor C_1 and T_1 twins, respectively. This study is the first to establish the statistical relevance of twin–twin junctions by collecting and processing data about all twinning modes and all twin–twin junctions in Zr. Six different types of twin–twin junctions, i.e. $T_1 - T_1, T_1 - T_2, T_1 - C_1, T_2 - T_2, T_2 - C_1$ and $C_1 - C_1$, are observed. Twin–twin junctions occurring between twins belonging to different modes, and more particularly between twins belonging to the first and second most active twinning modes, appear very frequently and cannot be neglected. Depending on the loading configuration, they may represent more than half of all twin–twin junctions. The comparison between the average twin thickness of twins embedded in single twinned and multi-twinned grains reveals that twin–twin junctions hinder twin growth. In addition, only nucleation and growth of twins belonging to the predominant twinning mode seem to be strongly sensitive to grain orientation and loading direction. These differences can probably be explained by the presence of localized high stress levels allowing the nucleation of any twinning mode. In agreement with previous studies, it is also found that the probability of twin nucleation and the average number of twins per twinned grain increase with grain size.

Appendix A

Fig. 15 consists in a graphical representation of twin–twin junction modes and types observed in TT03 and IP05 maps. Twins are represented via their twinning planes, K_1. Junctions such as $C_2 - C_2, C_2 - C_1, C_2 - T_2$ and $C_2 - T_1$ are not shown because not observed or statistically irrelevant.

References

[1] P.G. Partridge, The crystallography and deformation modes of hexagonal close-packed metals, Metall. Rev. 12 (118) (1967) 168–192.

[2] G.C. Kaschner, C.N. Tomé, I.J. Beyerlein, S.C. Vogel, D.W. Brown, R.J. McCabe, Role of twinning in the hardening response of zirconium during temperature reloads, Acta Mater. 54 (11) (2006) 2887–2896.

[3] R.J. McCabe, E.K. Cerreta, A. Misra, G.C. Kaschner, C.N. Tomé, Effects of texture, temperature and strain on the deformation modes of zirconium, Philos. Mag. 86 (23) (2006) 3595–3611.

[4] M.H. Yoo, Slip, twinning and fracture in hexagonal close-packed metals, Metall. Mater. Trans. A 12 (3) (1981) 409–418.

[5] M.H. Yoo, J.K. Lee, Deformation twinning in hcp metals and alloys, Philos. Mag. A Phys. Condens. Matter Struct. Defects Mech. Prop. 63 (5) (1991) 987–1000.

[6] C.N. Tomé, P.J. Maudlin, R.A. Lebensohn, G.C. Kaschner, Mechanical response of zirconiumi. Derivation of a polycrystal constitutive law and finite element analysis, Acta Mater. 49 (15) (2001) 3085–3096.

[7] E.J. Rapperport, Room temperature deformation processes in zirconium, Acta Metall. 7 (4) (1959) 254–260.

[8] E.J. Rapperport, C.S. Hartley, Deformation modes of zirconium at 77-degrees-k, 575-degrees-k, and 1075-degrees-k, Trans. Am. Inst. Min. Metall. Eng. 218 (5) (1960) 869–877.

[9] A. Akhtar, A. Teghtsoonian, Plastic deformation of zirconium single crystals, Acta Metall. 19 (7) (1971) 655–663.

[10] A.G. Crocker, The crystallography of deformation twinning in alpha-uranium, J. Nucl. Mater. 16 (3) (1965) 306–326.

[11] R.W. Cahn, Plastic deformation of alpha-uranium; twinning and slip, Acta Metall. 1 (1) (1953) 49–70.

[12] J.W. Christian, S. Mahajan, Deformation twinning, Progr. Mater. Sci. 39 (1–2) (1995) 1–157.

[13] A. Serra, D.J. Bacon, R.C. Pond, The crystallography and core structure of twinning dislocations in hcp metals, Acta Metall. 36 (12) (1988) 3183–3203.

[14] M.H. Yoo, S.R. Agnew, J.R. Morris, K.M. Ho, Non-basal slip systems in {HCP} metals and alloys: source mechanisms, Mater. Sci. Eng. A 319321 (2001) 87–92.

[15] M.H. Yoo, J.R. Morris, K.M. Ho, S.R. Agnew, Nonbasal deformation modes of hcp metals and alloys: Role of dislocation source and mobility, Metall. Mater. Trans. A 33 (3, SI) (2002) 813–822.

[16] N. Bertin, C.N. Tomé, I.J. Beyerlein, M.R. Barnett, L. Capolungo, On the strength of dislocation interactions and their effect on latent hardening in pure magnesium, Int. J. Plast. 62 (2014) 72–92.

[17] L. Capolungo, I.J. Beyerlein, C.N. Tomé, Slip-assisted twin growth in hexagonal close-packed metals, Scr. Mater. 60 (1) (2009) 32–35.

[18] L. Capolungo, I.J. Beyerlein, G.C. Kaschner, C.N. Tomé, On the interaction between slip dislocations and twins in HCP Zr, Mater. Sci. Eng. A 513514 (2009) 42–51.

[19] R.J. McCabe, G. Proust, E.K. Cerreta, A. Misra, Quantitative analysis of deformation twinning in zirconium, Int. J. Plast. 25 (3) (2009) 454–472.

[20] G. Proust, C. Tomé, G. Kaschner, Modeling texture, twinning and hardening evolution during deformation of hexagonal materials, Acta Mater. 55 (6) (2007) 2137–2148.

[21] A. Serra, D.J. Bacon, R.C. Pond, Dislocations in interfaces in the h.c.p. metals. Defects formed by absorption of crystal dislocations, Acta Mater. 47 (5) (1999) 1425–1439.

[22] I.J. Beyerlein, C.N. Tomé, A dislocation-based constitutive law for pure Zr including temperature effects, Int. J. Plast. 24 (5) (2008) 867–895.

[23] G. Monnet, B. Devincre, L.P. Kubin, Dislocation study of prismatic slip systems and their interactions in hexagonal close packed metals: application to zirconium, Acta Mater. 52 (14) (2004) 4317–4328.

[24] P.-A. Juan, S. Berbenni, M.R. Barnett, C.N. Tomé, L. Capolungo, A double inclusion homogenization scheme for polycrystals with hierarchal topologies: application to twinning in mg alloys, Int. J. Plast. 60 (2014) 182–196.

[25] H.E. Kadiri, J. Kapil, A. Oppedal, L.H. Jr, S.R. Agnew, M. Cherkaoui, S. Vogel, The effect of twin–twin interactions on the nucleation and propagation of twinning in magnesium, Acta Mater. 61 (10) (2013) 3549–3563.

[26] Q. Yu, J. Wang, Y. Jiang, R.J. McCabe, N. Li, C.N. Tomé, Twin twin interactions in magnesium, Acta Mater. 77 (2014) 28–42.

[27] Q. Yu, J. Wang, Y. Jiang, R.J. McCabe, C.N. Tomé, Co-zone {1012} twin interaction in magnesium single crystal, Mater. Res. Lett. 2 (2) (2014) 82–88.

[28] L. Capolungo, P.E. Marshall, R.J. McCabe, I.J. Beyerlein, C.N. Tomé, Nucleation and growth of twins in Zr: a statistical study, Acta Mater. 57 (20) (2009) 6047–6056.

[29] I.J. Beyerlein, L. Capolungo, P.E. Marshall, R.J. McCabe, C.N. Tome, Statistical analyses of deformation twinning in magnesium, Philos. Mag. 90 (16) (2010) 2161–2190.

[30] C. Pradalier, P.-A. Juan, L. Capolungo, A graph theory based automated twin recognition technique for electron backscatter diffraction analysis, Journal of Microscopy, submitted for publication.

[31] P.E. Marshall, G. Proust, J.T. Rogers, R.J. McCabe, Automatic twin statistics from electron backscattered diffraction data, J. Microsc. 238 (3) (2010) 218–229.

[32] D. Scott, On optimal and data-based histograms, Biometrika 66 (1979) 605–610.

[33] M.A. Kumar, A.K. Kanjarla, S.R. Niezgoda, R.A. Lebensohn, C.N. Tomé, Numerical study of the stress state of a deformation twin in magnesium, Acta Mater. 84 (2015) 349–358.

[34] Z.-Z. Shi, Y. Zhang, F. Wagner, P.-A. Juan, S. Berbenni, L. Capolungo, J.-S. Lecomte, T. Richeton, On the selection of extension twin variants with low schmid factors in a deformed mg alloy, Acta Mater. 83 (2015) 17–28.